We are IntechOpen, the world's leading publisher of Open Access books Built by scientists, for scientists

4,800
Open access books available

122,000
International authors and editors

135M
Downloads

Our authors are among the

154
Countries delivered to

TOP 1%
most cited scientists

12.2%
Contributors from top 500 universities

BOOK CITATION INDEX
CLARIVATE ANALYTICS
INDEXED

WEB OF SCIENCE™

Selection of our books indexed in the Book Citation Index
in Web of Science™ Core Collection (BKCI)

Interested in publishing with us?
Contact book.department@intechopen.com

Gait Generation of Multilegged Robots by using Hardware Artificial Neural Networks

Ken Saito, Masaya Ohara, Mizuki Abe,
Minami Kaneko and Fumio Uchikoba

Abstract

Living organisms can act autonomously because biological neural networks process the environmental information in continuous time. Therefore, living organisms have inspired many applications of autonomous control to small-sized robots. In this chapter, a small-sized robot is controlled by a hardware artificial neural network (ANN) without software programs. Previously, the authors constructed a multilegged walking robot. The link mechanism of the limbs was designed to reduce the number of actuators. The current paper describes the basic characteristics of hardware ANNs that generate the gait for multilegged robots. The pulses emitted by the hardware ANN generate oscillating patterns of electrical activity. The pulse-type hardware ANN model has the basic features of a class II neuron model, which behaves like a resonator. Thus, gait generation by the hardware ANNs mimics the synchronization phenomena in biological neural networks. Consequently, our constructed hardware ANNs can generate multilegged robot gaits without requiring software programs.

Keywords: hardware artificial neural networks, pulse-type hardware neuron model, gait, multilegged robot, MEMS, link mechanism, class II neuron model, synchronization phenomena

1. Introduction

Many types of multilegged robots have been developed for various applications [1–3]. Most of these robots were bioinspired by the structures, features, and excellent functionalities of living organisms [4, 5]. Living organisms autonomously operate under the control of small-sized neural networks. Therefore, researchers have begun studying artificial neural networks (ANNs) for robot control [6–10]. Biological neural networks are universally characterized by oscillatory patterns of electrical activity. These patterns govern several functions of living organisms, such as heart rhythms, movements, and swallowing [11, 12]. The oscillatory patterns

of living organisms can be clarified through coupled neuron models, which have two categories: class I and class II [13]. Given that the class II model is more easily synchronized than the class I model, the class II model is applied in studies of synchronization phenomena. Famous class II neuron models include the Hodgkin-Huxley model [14] and Bonhoeffer-van der Pol model [15], mathematical neuron models that form the basis of bioinspired oscillatory pattern generation [16–18]. Most of the central pattern generators (CPGs) designed for the synchronized locomotion control of multilegged robots [6–8] are also constructed by mathematical neuron models. A CPG model using mathematical neuron models can be implemented on a field programmable gate array (FPGA). However, an FPGA board cannot be mounted on a millimeter-sized robot system because of its size. Instead, oscillatory patterns for very small robots can be generated by hardware neuron models. Hardware rings of coupled oscillators, which can generate various oscillatory patterns by using the synchronization phenomena [19, 20], have been employed as the structural elements of ANNs. However, given that most of the hardware neuron models contain inductors in their circuit architectures [19–22], they are difficult to implement in an integrated circuit (IC); thus, the use of such models is disadvantageous on the circuit scale [23]. In particular, ICs can be combined with mechanical parts of the robot by using microelectromechanical system (MEMS) technology, which can reduce the robot size to the millimeter scale.

The authors are studying hardware ANNs based on a pulse-type hardware neuron model [24–27] with the same basic features as biological neurons. Specifically, this model possesses spatiotemporal summation characteristics, a threshold period, and a refractory period and generates oscillating patterns of electrical activity. Furthermore, the pulse-type hardware neuron model requires no inductors; therefore, the system is easily implemented in an IC.

Previously, the authors proposed two types of prototype multilegged robots: a quadruped robot approximately 10 cm in size [26] and a hexapod robot approximately 5 mm in size [27]. Both multilegged robots move their limbs by stepping motions. A multilegged robot usually needs actuators for each joint. In our multilegged robots, the number of actuators is reduced by a link mechanism, and the gait is controlled by a hardware ANN. The hardware ANN consists of 4 excitatory synaptic models, 16 inhibitory synaptic models, and 8 cell body models for the quadruped robot [26], and 12 inhibitory synaptic models and 4 cell body models for the hexapod robot [27–29].

This chapter describes the basic characteristics of the hardware ANNs that generate the gait of multilegged robots. After briefly introducing both types of multilegged robots, it discusses the hardware ANNs and mathematically describes the characteristics of the pulse-type hardware neuron model. The oscillation characteristic of the model requires a negative resistance and is described in a phase plane. The synchronization characteristics of connected hardware ANNs are also discussed. Finally, the hardware ANNs are validated in locomotion tests of the multilegged robot.

2. Multilegged robots

The quadruped and hexapod robots have been described in previous works [26, 27]. This section briefly introduces the mechanical components of the fabricated multilegged robots.

2.1. Quadruped robot

The width, length, and height dimensions of the quadruped robot are 130, 140, and 90 mm, respectively (see **Figure 1**). The quadruped robot is constructed from mechanical and electrical components. The mechanical components comprise the body frame, four servo motors, link mechanisms, and four legs. The electrical components consist of the control board, hardware ANNs, and battery. The limbs and body frame are made from aluminum base alloy 2017 and aluminum base alloy 5052, respectively. The mechanical parts are fabricated by a computerized numerical control machining system. The four legs of the quadruped robot system are actuated by four servo motors, and the stepping motion of each leg is generated by the link mechanisms. The servo motor is an HSR-8498HB (Hitec Multiplex Japan) model, which generates sufficient maximum torque to actuate the robot. The mechanical components of the quadruped robot are detailed in [26].

Figure 2 shows the relative phase difference of the quadruped gait pattern under a given driving rhythm of the actuators. The relative phase difference is referenced to the left forelimb (0°). Under various actuation rhythms, the quadruped robot generates different gait patterns. **Figure 2** displays five typical gait patterns: walk, trot, pace, bound, and gallop. The directional changes and turning of the quadruped robot are not realized at present. The robot gait is easily controlled by software programs implemented on a control board. However, in the proposed robot control, the software program for generating the locomotion rhythms is replaced by a hardware ANN.

2.2. Hexapod robot

The fabricated hexapod robot is displayed in **Figure 3**. The robot is 4.0 mm wide, 2.7 mm long, and 2.5 mm high. Two ground (GND) wires and eight signal wires (all made of copper) extend above the robot. The hexapod robot walks when the signal wires are connected to the hardware ANNs. The structure and stepping motion of the robot mimic those of an ant. The ant-like stepping motion is a series of tripod configurations in which two groups of three legs alternate between swing and stance phases (see **Figure 5** in [29]). The hexapod robot comprises
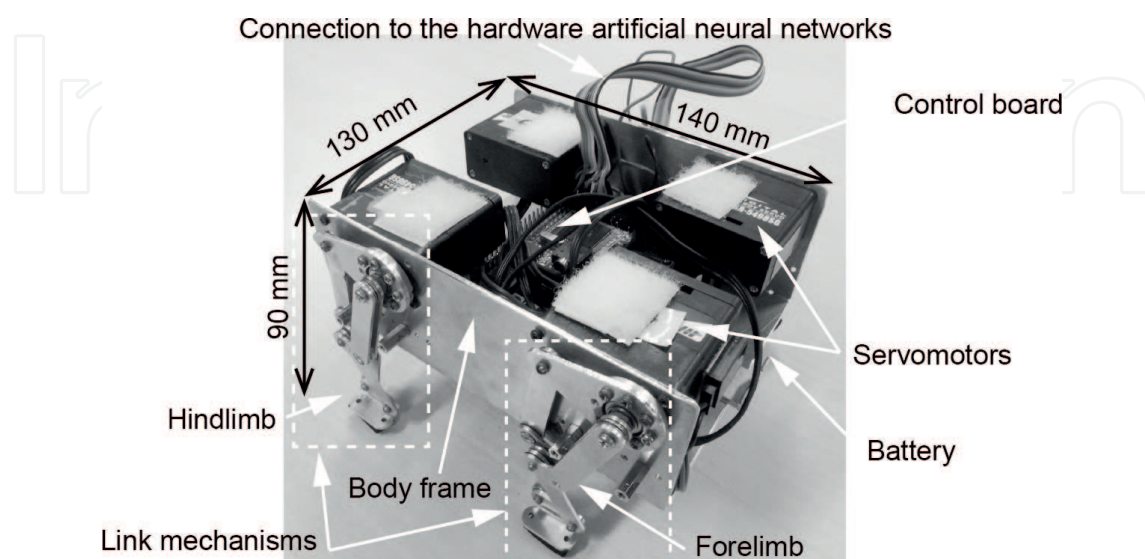

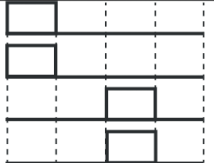**Figure 1.** Image of the constructed quadruped robot.
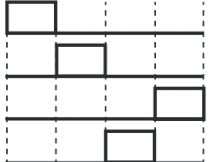
Gait pattern	Leg	Phase difference				Driving rhythm
		0°	90°	180°	270°	
Walk	LF	D				
	RF			D		
	LH				D	
	RH		D			
Trot	LF	D				
	RF			D		
	LH			D		
	RH	D				
Pace	LF	D				
	RF			D		
	LH	D				
	RH			D		
Bound	LF	D				
	RF	D				
	LH			D		
	RH			D		
Gallop	LF	D				
	RF		D			
	LH				D	
	RH			D		

Figure 2. Relative phase difference of quadruped gait patterns for different driving rhythms of the actuators. LF, RF, LH, and RH refer to left forelimb, right forelimb, left hindlimb, and right hindlimb, respectively.

the frame parts, small-sized actuators, and link mechanisms. The small-sized actuators are constructed from artificial muscle wire. All mechanical parts are made from silicon wafers of various thicknesses (100, 200, 385, and 500 μm). The parts were shaped by dry etching by photolithography-based inductively coupled plasma [30]. The small-sized actuator consists of four pieces of artificial muscle wire, as well as the shaft, rotor, and GND wire. The frame components and rotors are connected by the artificial muscle wire, which functions as a shape memory alloy [31]. The artificial muscle wire is BMX50 (BioMetal® Helix, available online at http://www.toki.co.jp [32]). The mechanical components of the hexapod robot are detailed in previous works [27, 29].

Figure 4 shows the leg motions of the hexapod robot. The artificial muscle wire shrinks at high temperatures and extends at low temperatures. Therefore, when an electric current is applied through the wire, the resulting heat displaces the four pieces of artificial muscle wire, and the rotor rotates. The wire is cooled by stopping the current flow. Thus, the actuator is rotated by changing the sequence of the input current. The link mechanism transmits the rotational movements of the rotor to the three legs on one side. This design requires only two small-sized actuators (one on each side of the robot) to actuate the six legs.
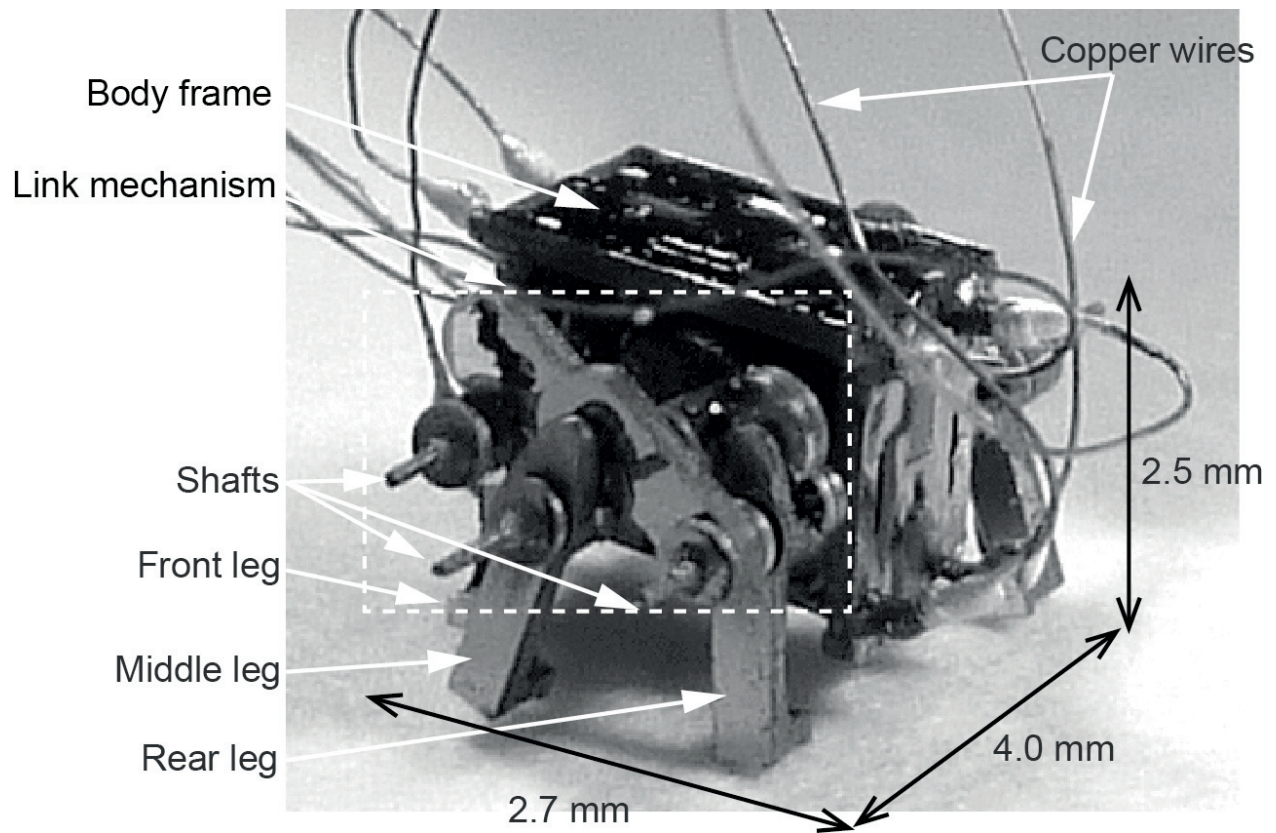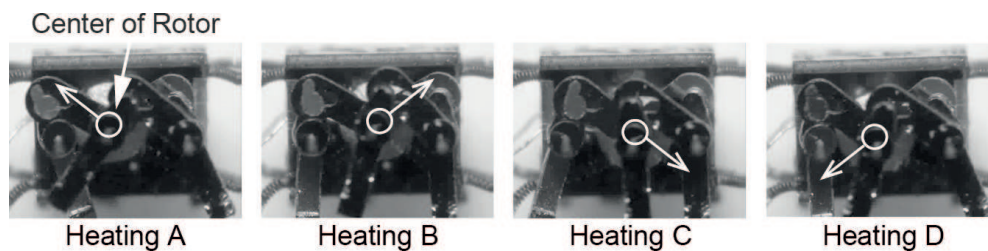
Figure 3. Image of the constructed hexapod robot.

Figure 4. Leg motions of the hexapod robot.

Gait pattern	Wire	0°	90°	180°	270°	Driving rhythm
			Phase difference			
Forward walk	A	D				
	B		D			
	C			D		
	D				D	
Backward walk	A				D	
	B			D		
	C		D			
	D	D				

Figure 5. Relative phase difference of hexapod gait patterns for different driving rhythms of the actuator.

Figure 5 shows the relative phase differences of the hexapod gait patterns for different driving rhythms of the actuator. To heat the artificial muscle wires, an input pulse of amplitude 50–100 mA, period 2 s, and width 0.5 s is required. Therefore, the hexapod robot requires 2 s to complete one locomotion cycle. As mentioned above, the length of the artificial muscle wire depends on the temperature. Specifically, the wire shrinks when heated and extends when cooled. Heating the artificial muscle wires from A to D and from D to A in **Figure 4** drives the hexapod robot forward and backward, respectively. The locomotion pattern is a 180° phase shift at each side, which mimics locomotion of an ant. If the input pulse is narrower than 0.5 s, the thermal heating by the driving current is insufficient to shrink the wire. By contrast, if the input pulse is wider than 2 s, the thermal heating by the driving current is excessive, and the cooling is insufficient to extend the wire.

3. Hardware artificial neural networks

The hardware ANNs are based on a pulse-type hardware neuron model of class II, specifically, a Hodgkin-Huxley model and a Bonhoeffer-van der Pol model [28]. This section describes the circuit diagrams and the basic characteristics of the pulse-type hardware neuron model. The synchronization phenomena of the hardware ANNs are also discussed.

3.1. Pulse-type hardware neuron model

Figure 6 shows the circuit diagrams of the pulse-type hardware neuron model, which comprises a cell body model and two synaptic models. The cell body model (**Figure 6a**) includes a voltage control-type negative resistance, an equivalent inductance, resistors R_1 and R_2, and a membrane capacitor C_M. The voltage control-type negative resistance circuit with equivalent inductance consists of an n-channel MOSFET M_1, a p-channel MOSFET M_2, a voltage source V_A, a leak resistor R_L, another resistor R_G, and a capacitor C_G. The cell body model generates oscillating patterns of electrical activity v_M (t). v_G (t) is the voltage between both ends of
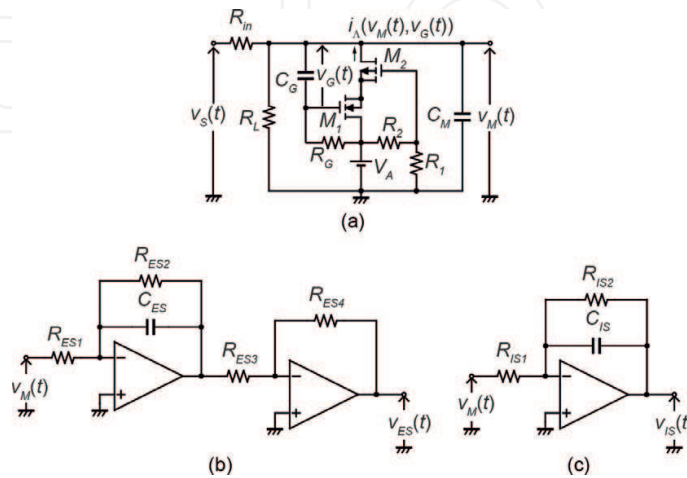

Figure 6. Circuit diagram of the pulse-type hardware neuron model. (a) Cell body model, (b) excitatory synaptic model, and (c) inhibitory synaptic model.

capacitor C_G. $v_M(t)$ and $v_G(t)$ are, respectively, governed by the following simultaneous differential equations.

$$C_M \frac{dv_M(t)}{dt} = \frac{v_s(t)}{R_{in}} - \frac{v_M(t)}{R_L} - \frac{v_M(t) - v_G(t) - V_A}{R_G} + i_\Lambda(v_M(t), v_G(t)), \tag{1}$$

$$C_G \frac{dv_G(t)}{dt} = \frac{v_M(t) - v_G(t) - V_A}{R_G}. \tag{2}$$

A time-dependent nonlinear current $i_\Lambda(v_M(t),v_G(t))$ flows through the negative resistance circuit. The governing equations of $i_\Lambda(v_M(t),v_G(t))$ under the three possible conditions are given by the following:

$$\text{Condition 1} : v_G(t) + V_A + V_{Tn} + V_{Tp} < v_M(t) \leq V_{Gp} + V_{Tp},$$

$$i_\Lambda(v_M(t), v_G(t)) = \frac{\beta}{8}(A + B + V_{Gp})^2 \tag{3}$$

$$\text{Condition 2} : V_{Gp} + V_{Tp} < v_M(t) \leq v_G(t) + V_A + V_{Tn},$$

$$i_\Lambda(v_M(t), v_G(t)) = \frac{\beta \cdot A^2 (A - 2(B + V_{Gp}))^2}{8(A + B + V_{Gp})^2} \tag{4}$$

$$\text{Condition 3} : v_G(t) + V_A + V_{Tn} < v_M(t) \leq V_A,$$

$$i_\Lambda(v_M(t),v_G(t)) =$$
$$\frac{\beta\{(V_A - v_M(t))(V_A - v_M(t) + 2A)(V_A + v_M(t) - 2(V_{Tp} + V_{Gp}))(V_A - 3v_M(t) + 2(V_{Tp} + A + V_{Gp}))\}}{8(A + B + V_{Gp})^2}$$

$$\tag{5}$$

where $A = v_G(t) + V_{Tn}, B = V_{Tp} - v_M(t), V_{Gp} = \frac{V_A \cdot R_2}{R_1 + R_2}, \frac{\beta}{2} = \frac{\mu \varepsilon W}{2t L}$, and V_{Tn} and V_{Tp} are the threshold voltages of the n and p-channel MOSFETs, respectively. V_{Gp} is the gate voltage of MOSFET M_2. β is the conductance constant of the MOSFETs (with carrier mobility μ, dielectric constant ε of the gate insulator, oxide channel thickness t, channel width W and channel length L). Although the value of β differs in the n-type and p-type MOSFETs, Eqs. (3–5) become intractable unless the βs are approximated by the same value. The complex case with different βs is considered in the following numerical analysis.

The circuit parameters of the cell body model are as follows: $C_G = 4.7\ \mu F$, $C_M = 470\ nF$, $R_G = 680\ k\Omega$, $R_L = 10\ k\Omega$, $R_1 = 15\ k\Omega$, $R_2 = 20\ k\Omega$, and $R_{in} = 50\ k\Omega$. The voltage source $V_A = 3.5\ V$. The authors have used the BSS83 and BSH205 for M_1 and M_2, respectively. These circuit parameters are set to allow the cell body model to generate oscillation with amplitude 3.5 V, period 8 s, and width of 2 s.

Figure 6b and **c** displays the circuits of the excitatory and inhibitory synaptic models, respectively. The spatiotemporal summation characteristics of the synaptic model resemble those of biological systems. The output $v_S(t)$ of the synaptic model is the spatiotemporal summation of the output voltages of the cell body model $v_M(t)$. $v_{ES}(t)$ and $v_{IS}(t)$ are described by the following equations.

$$v_{ES}(t) = \frac{R_{ES2}}{R_{ES1}} \cdot \frac{R_{ES4}}{R_{ES3}} \left(1 - e^{-\frac{t}{R_{ES2} \cdot C_{ES}}}\right) \cdot v_M(t), \tag{6}$$

$$v_{IS}(t) = -\frac{R_{IS2}}{R_{IS1}} \left(1 - e^{-\frac{t}{R_{IS2} \cdot C_{IS}}}\right) \cdot v_M(t). \tag{7}$$

The spatial summation is performed by the inverting amplifier, whose amplification factor imitates the synaptic weight. Suffixes E and I denote excitatory and inhibitory, respectively. The temporal summation is realized by the operational amplifier RC integrator. The resistors and capacitors in the synaptic model are valued at 1 MΩ and 1 pF, respectively. The operational amplifier is an RC4558D.

3.2. Basic characteristics of the cell body model

Figure 7 shows the negative resistance characteristics of the cell body model. The N-shape characteristic indicates that the negative resistance is voltage control type negative resistance. When $2.3 < v_M(t) < 3.5$ ($v_G(t) = 2.5$ V), the negative resistance is provided by the negative resistance circuit. The amplitude of the negative resistance characteristic can be changed by varying the $v_G(t)$.

Figure 8 shows the phase plane of the cell body model. The attractor (solid line in **Figure 8**) is the limit cycle. The shapes of the $v_M(t)$- and $v_G(t)$-nullclines confirm the class II neuron characteristics of the cell body model. The same characteristics are observed in the Hodgkin-Huxley and Bonhoeffer-van der Pol models. The $v_M(t)$- and $v_G(t)$-nullclines intersect at the equilibrium point. When the equilibrium point $dv_M/dv_G > 0$, the cell body model becomes unstable and self-oscillates. By contrast, when $dv_M/dv_G < 0$, the cell body model becomes stable. In this chapter, the equilibrium point is set to the unstable condition $dv_M/dv_G > 0$. The unstable and stable conditions can be switched by varying V_A.

3.3. Excitatory-inhibitory neuron pair model

The excitatory-inhibitory neuron pair model comprises two cell body models and two synaptic models and generates several oscillatory patterns by using the synchronization phenomena.
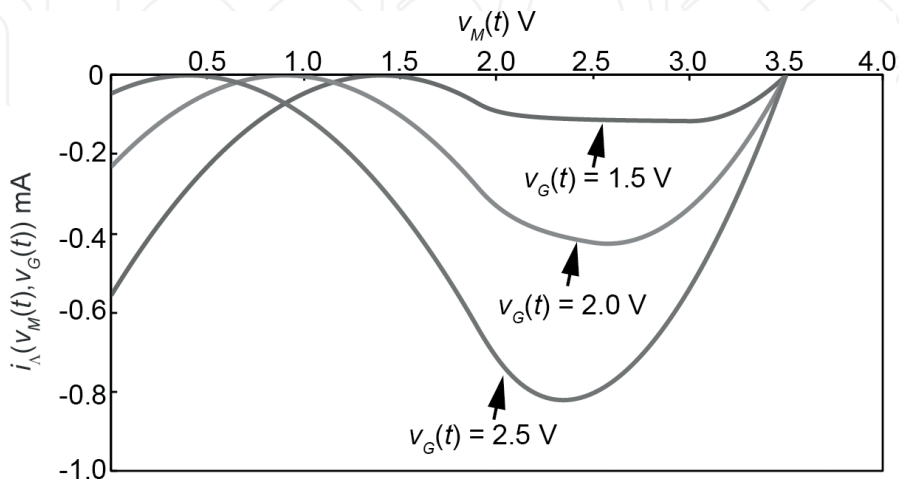

Figure 7. Negative resistance characteristic of the cell body model. The abscissa is $v_M(t)$ and the ordinate is $i_A(v_M(t), v_G(t))$.

Figure 9 shows the circuit diagram of the excitatory-inhibitory neuron pair model. The cell body models are mutually coupled by the synaptic models. The excitatory synaptic model sums the excitatory inputs (output voltage of the cell body model v_{ME} and the external input voltage v_{extinE}). Meanwhile, the inhibitory synaptic model sums the inhibitory inputs (output voltage of the cell body model v_{MI} and the external input voltage v_{extinI}). Both cell body models are assigned the same circuit parameters (The synchronization phenomena and oscillatory patterns of the mutually coupled excitatory-inhibitory neuron pair model are provided in [28]).
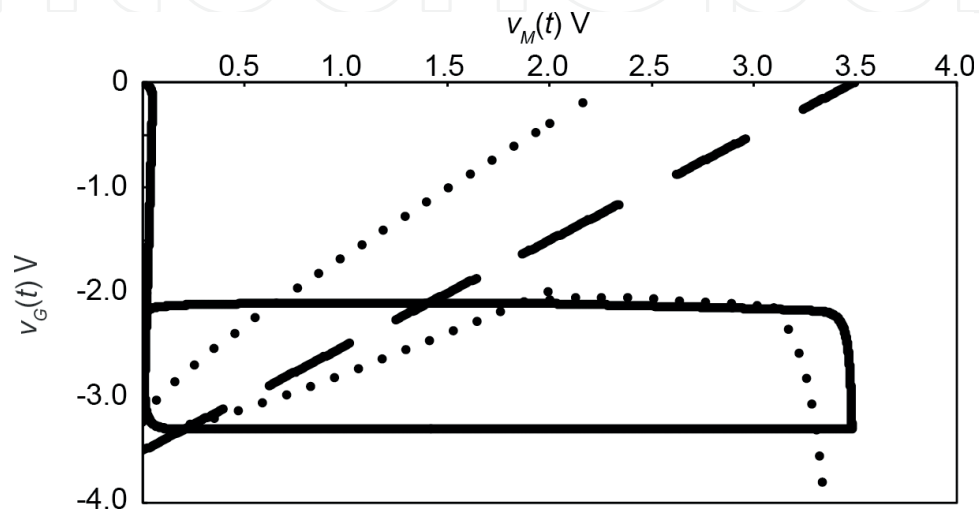
Figure 8. Phase plane of the cell body model. The abscissa is $vM(t)$ and the ordinate is $vG(t)$. The dotted, broken, and solid lines display the $vM(t)$-nullcline, $vG(t)$-nullcline, and attractor, respectively.
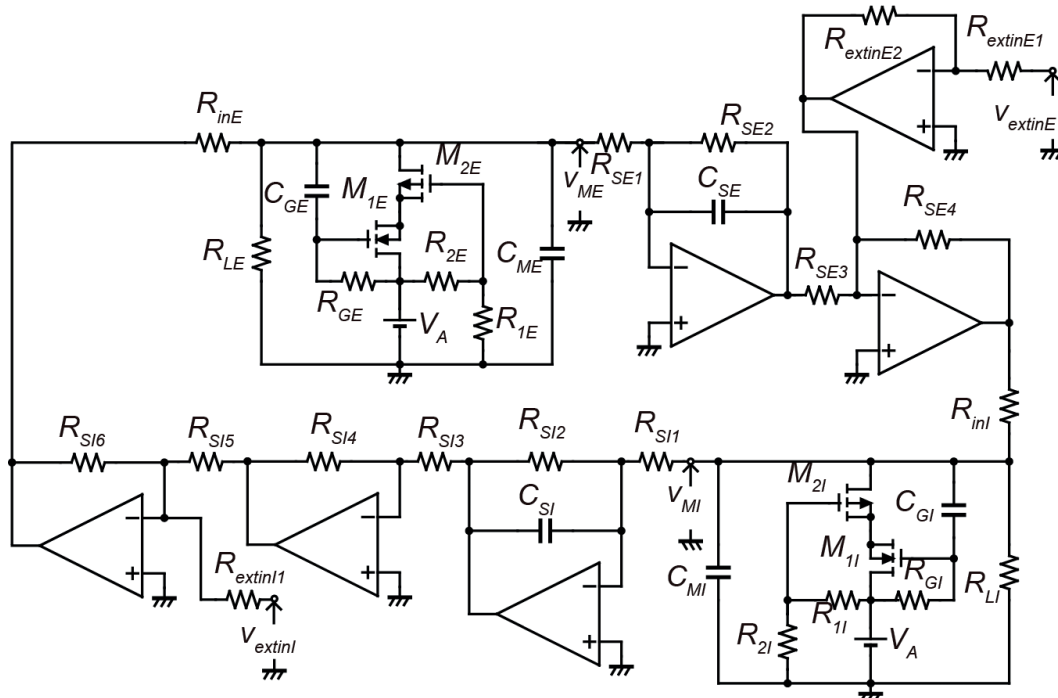

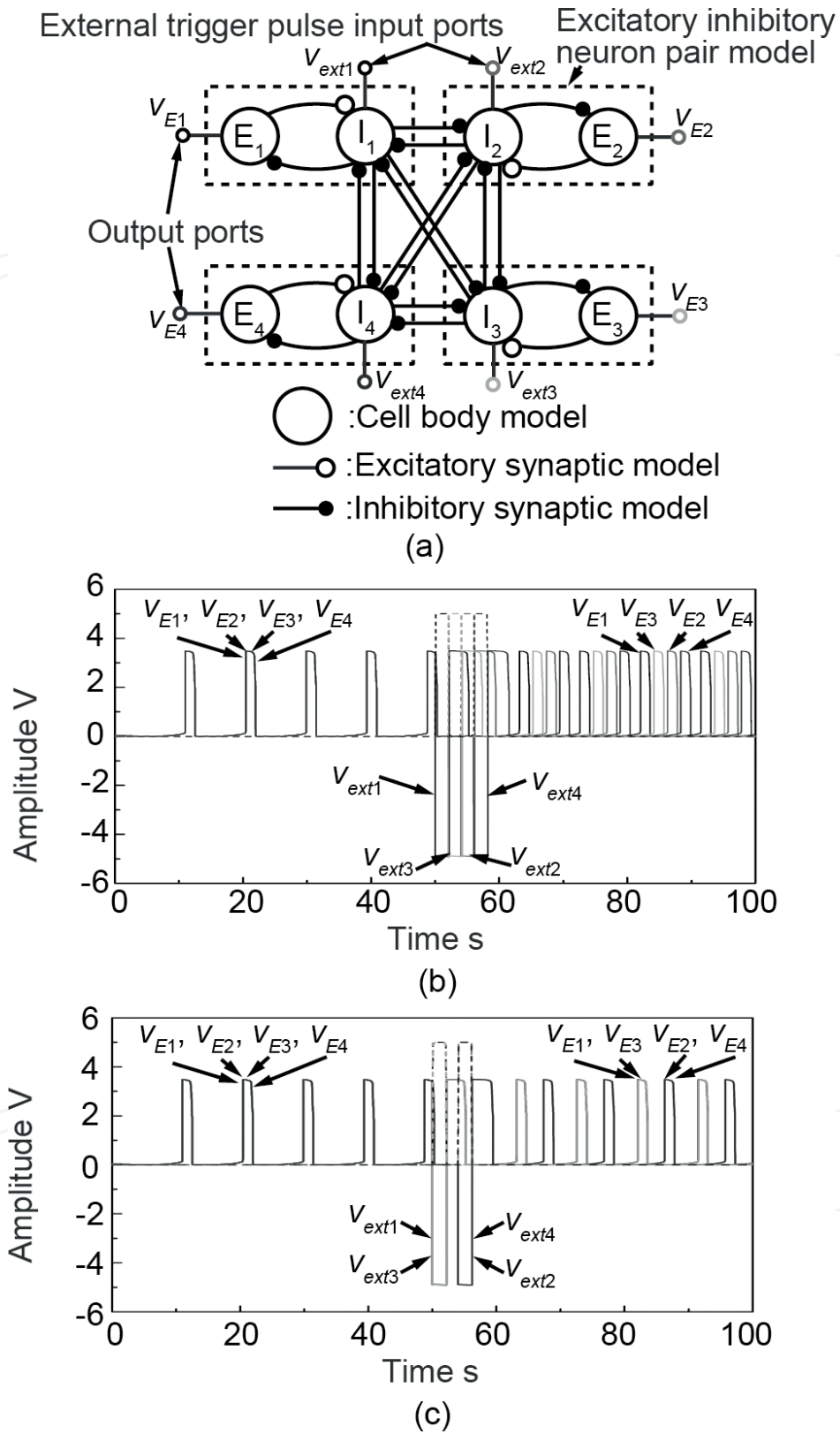**Figure 9.** Circuit diagram of the excitatory-inhibitory neuron pair model.

Figure 10. Four sets of excitatory-inhibitory neuron pair models connected by an inhibitory synaptic model. (a) Connection diagram, (b) output waveform when the external trigger pulse generates a walk sequence, (c) output waveform when the external trigger pulse generates a trot sequence (The waveforms in panels (b) and (c) are the simulation results).

The synchronization phenomena of the excitatory-inhibitory neuron pair circuit depend on the connection type of the synaptic model. When the synaptic model connection is excitatory or inhibitory, the synchronization is in-phase and anti-phase, respectively. The excitatory-inhibitory neuron pair circuit was incorporated into the hardware ANN for the quadruped robot.

3.4. Hardware neural networks for quadruped robot

Figure 10 shows the four sets of the excitatory-inhibitory neuron pair model connected by an inhibitory synaptic model. **Figure 10a** shows the connection diagram, and **Figure 10b** and **c** shows the output waveforms during the walking and trotting sequences in **Figure 2**, respectively. The motion sequences are initiated by an external trigger pulse. These results show that to generate a locomotion rhythm of the quadruped robot, the four sets of the excitatory-inhibitory neuron pair model must be connected to the inhibitory synaptic model. The sequences of the gait pattern differ between walk and gallop and between pace/bound and trot. The sequences are easily changed by changing the external trigger pulse.

3.5. Hardware neural networks for hexapod robot

Figure 11 shows the circuit diagrams of the pulse-type hardware neuron model with CMOS circuit. Given that circuit of **Figure 6** is difficult to construct in an IC with a limited layout area, it
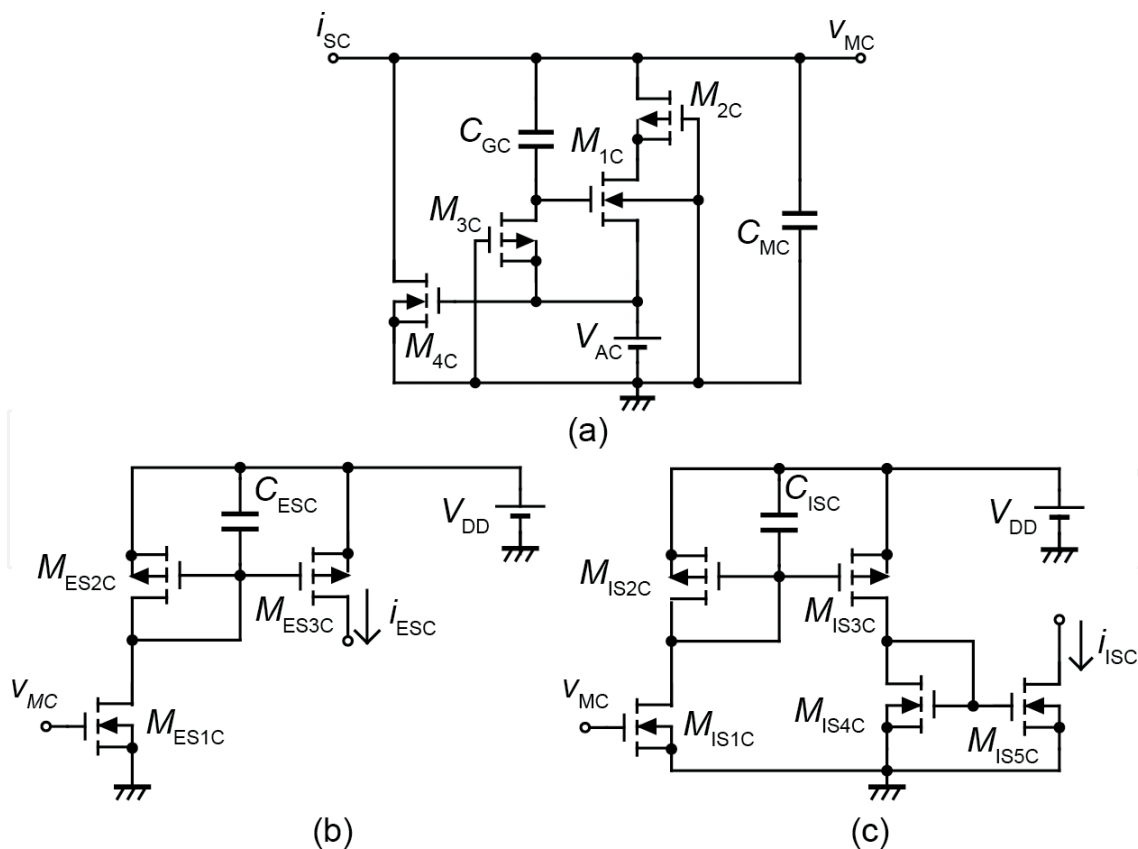

Figure 11. Circuit diagram of the pulse-type hardware neuron model (equivalent CMOS circuit). (a) Cell body model, (b) excitatory synaptic model, and (c) inhibitory synaptic model.

is replaced by a CMOS with an equivalent circuit. In the CMOS circuit, R_L and R_G in **Figure 6a** become the MOS resistors M_{4C} and M_{3C}, respectively. Furthermore, the operational amplifier is replaced by a simple current mirror circuit. However, the basic characteristics of **Figure 11** are unaffected by changing the circuit elements. The circuit parameters are $C_{GC} = 10\ \mu F$, $C_{MC} = 2.2\ \mu F$, M_{1C}, M_{2C}: $W/L = 10$, M_{3C}: $W/L = 0.1$, and M_{4C}: $W/L = 0.3$ for the cell body model and $C_{ESC} = C_{ISC} = 1\ pF$, $M_{ES1C\text{-}3C}$, and $M_{IS1C\text{-}5C}$: $W/L = 1$ for the synaptic model. The voltage sources of the cell body and synaptic models are $V_{AC} = 3.0\ V$ and $V_{DD} = 3.0\ V$, respectively.

Figure 12a shows the connection diagram of the inhibitory mutual coupling in the pulse-type hardware neuron model. Four sets of the model are coupled by 12 inhibitory synaptic models. **Figure 12b** shows a typical output waveform of the equivalent CMOS circuit. The inhibitory mutual coupling generates anti-phase synchronization, thus confirming that this coupling will achieve four anti-phase synchronizations. However, the random sequence of the output waveforms must be corrected to the repetitive sequence as shown in **Figure 5**. The correction is made by applying a single external trigger pulse.
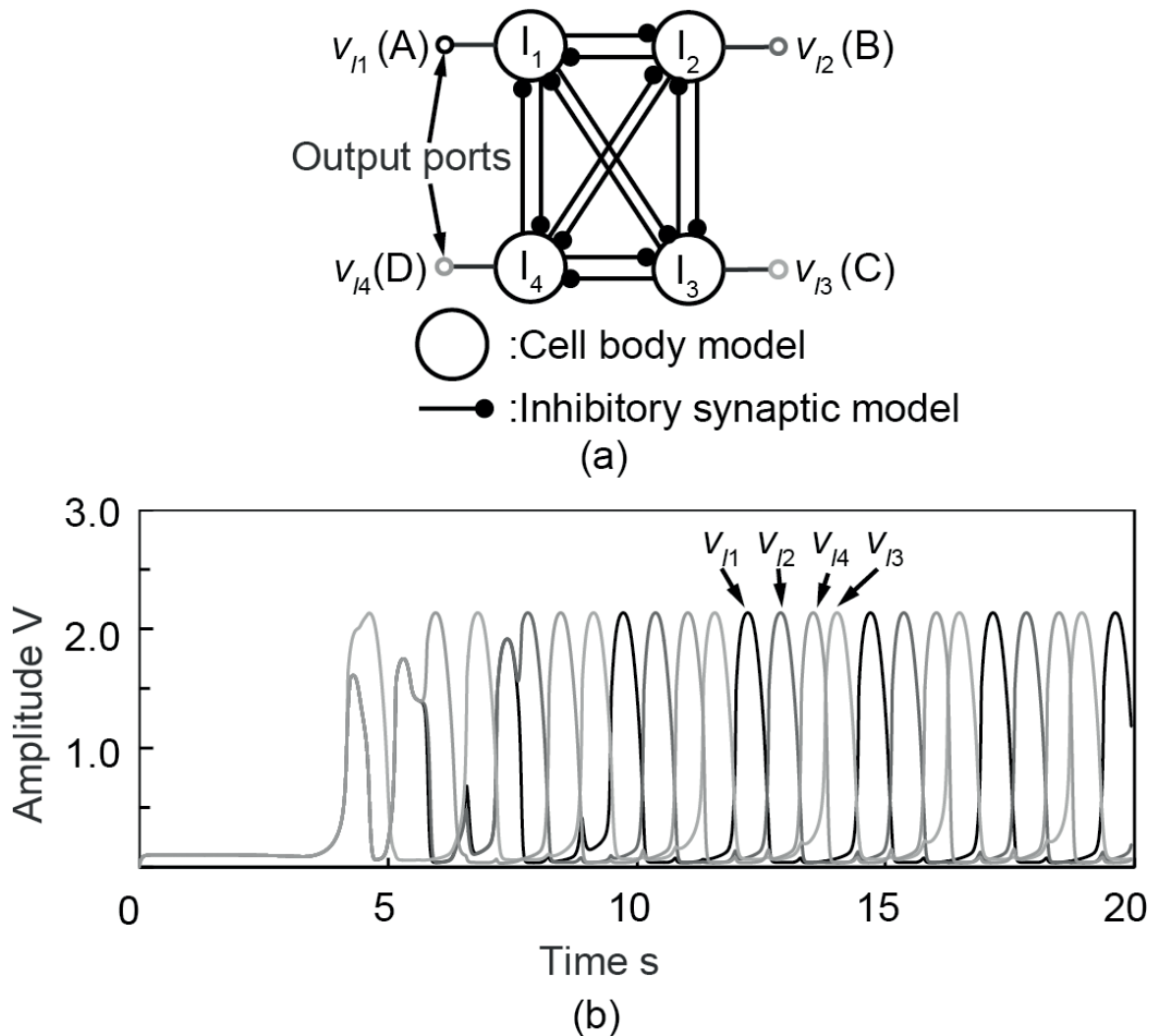

Figure 12. Inhibitory mutual coupling of four pulse-type hardware neuron models. (a) Connection diagram of inhibitory mutual coupling and (b) simulated output waveform of the CMOS equivalent circuit (anti-phase synchronization).
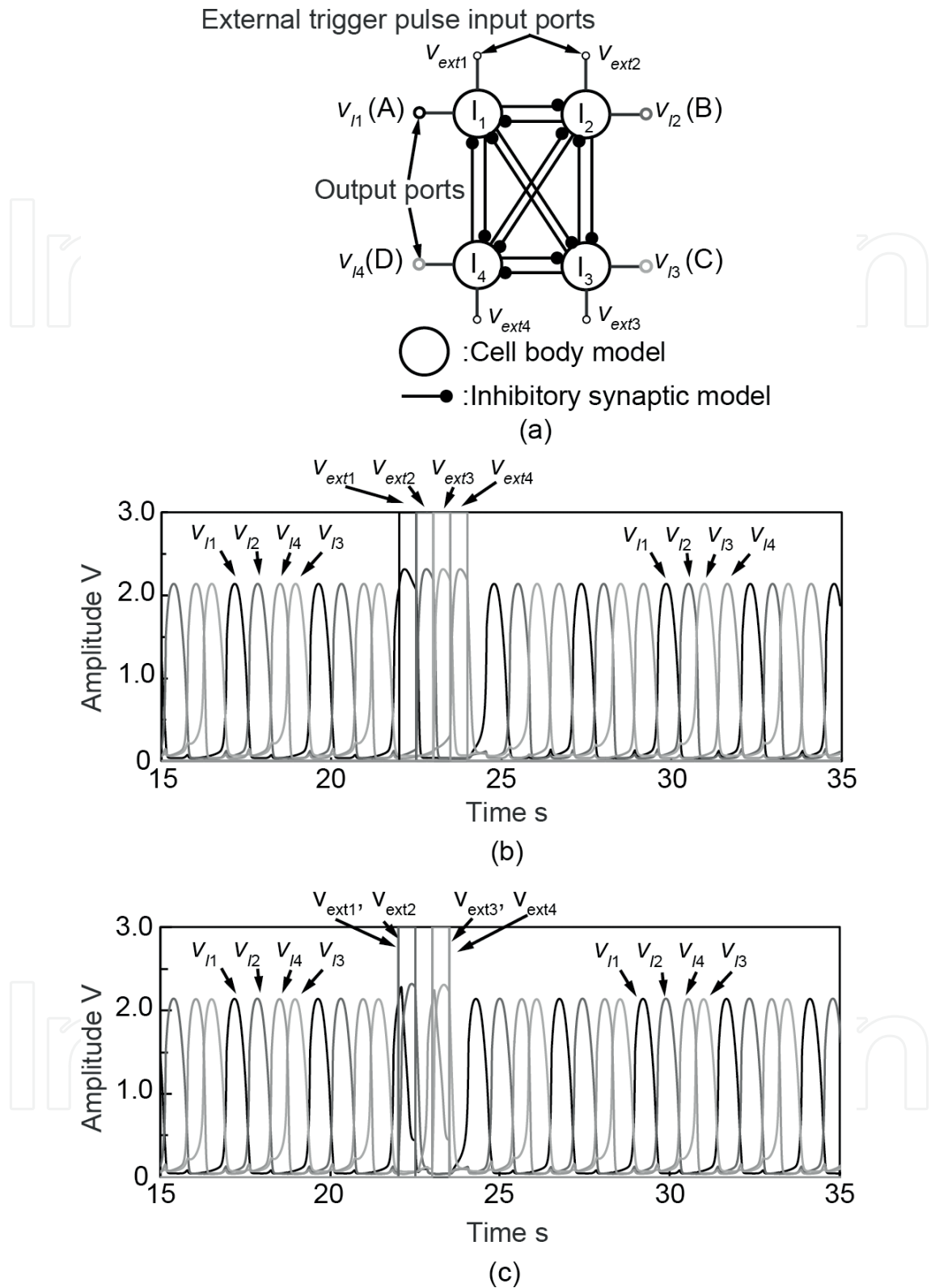
Figure 13. Applying the external trigger pulse to inhibitory mutual coupling of pulse-type hardware neuron models corrected by an external trigger pulse. (a) Connection diagram of inhibitory mutual coupling, (b) output waveform under an external trigger pulse (forward walk sequence in **Figure 5**), and (c) output waveform under an external trigger pulse (bound sequence in **Figure 2**). The waveforms in panels (b) and (c) are simulation results.

Figure 13 shows the inhibitory mutual coupling of the pulse-type hardware neuron models subjected to a single external trigger pulse. (a) The connection diagram of this system, and (b) a typical output waveform under the sequence v_{ext1}, v_{ext2}, v_{ext3}, and v_{ext4} of the trigger pulse (the forward walk sequence in **Figure 5**). Before applying the external trigger pulse, the output sequence was v_{I1}, v_{I2}, v_{I4}, and v_{I3}. After applying the pulse, it was corrected to v_{I1}, v_{I2}, v_{I3}, and v_{I4}. Therefore, the single-pulse correction realizes the forward and backward locomotion patterns in **Figure 5**. Note that walking and galloping in **Figure 2** and forward and backward locomotion patterns in **Figure 5** are all realized by the four-phase alternating oscillation and differ only in the order of their output sequences. **Figure 13c** shows a typical output waveform when the sequence of the external trigger pulse is v_{ext1}, v_{ext2} and (simultaneously) V_{ext3}, V_{ext4} (the bound sequence in **Figure 2**). The bound sequence is not realized by the external trigger pulse. The inhibitory mutual coupling of the pulse-type hardware neuron model cannot by itself generate the locomotion patterns of trot, pace, and bound because these motions are two-phase alternating oscillations.

4. Results and discussion

In this section, the gait rhythms generated by the hardware ANNs are tested in a multilegged robot.

4.1. Locomotion of the quadruped robot

Figure 14 shows the discrete circuits of the hardware ANNs. The electrical components were mounted on a frame-retardant type 4 (FR4) circuit board (The circuit diagram is shown in **Figures 6** and **9**.) The hardware ANN consisted of four sets of an excitatory-inhibitory neuron
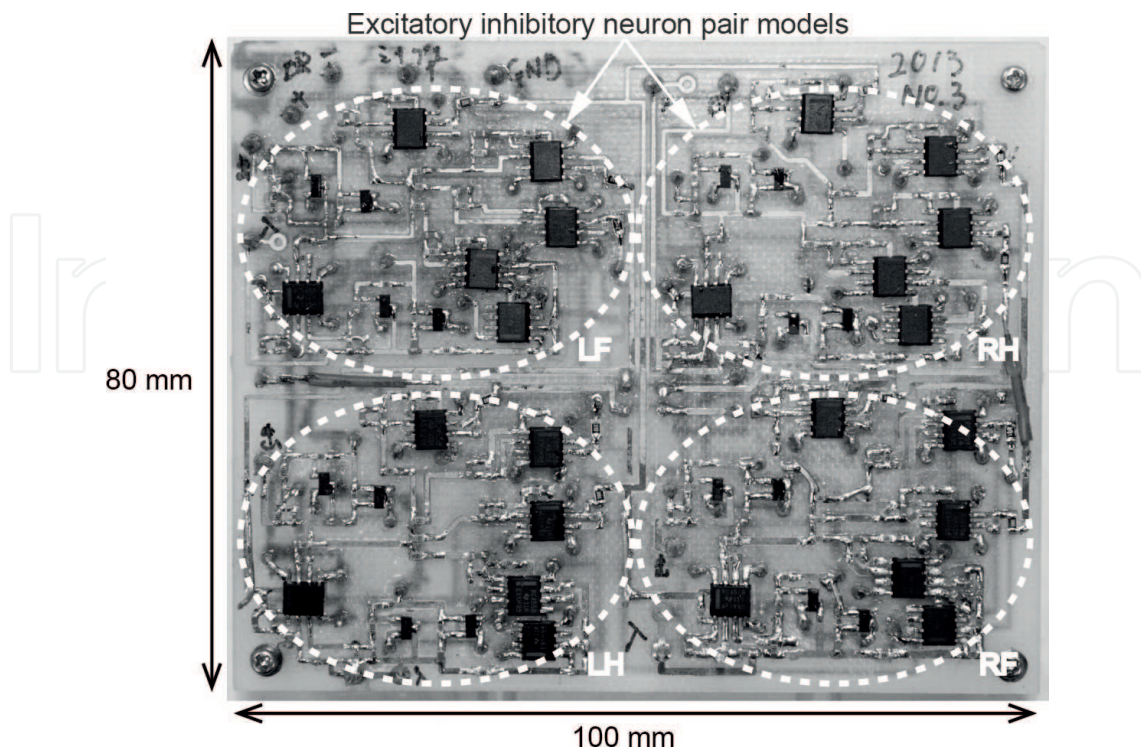

Figure 14. The hardware ANNs are constructed as discrete circuits.

pair model connected as shown in **Figure 10a**. The width and length of the mounted hardware ANNs are 100 and 80 mm, respectively; therefore, the hardware ANNs are sufficiently small to install on the quadruped robot.

Figure 15 shows the quadruped robot mounted with the hardware ANN circuit board. The quadruped robot system is 130 mm wide, 140 mm long, 100 mm high, and 530 g in weight. The power consumption of the hardware ANNs was approximately 360 mWh.

Walk sequence is the basic motion of the quadruped robot. **Figure 16** shows the generated gait pattern and leg motion of a quadruped robot. Panels (a) and (b) show the driving rhythm of the (measured) walking gait pattern and the leg motion of the robot, respectively. Under the
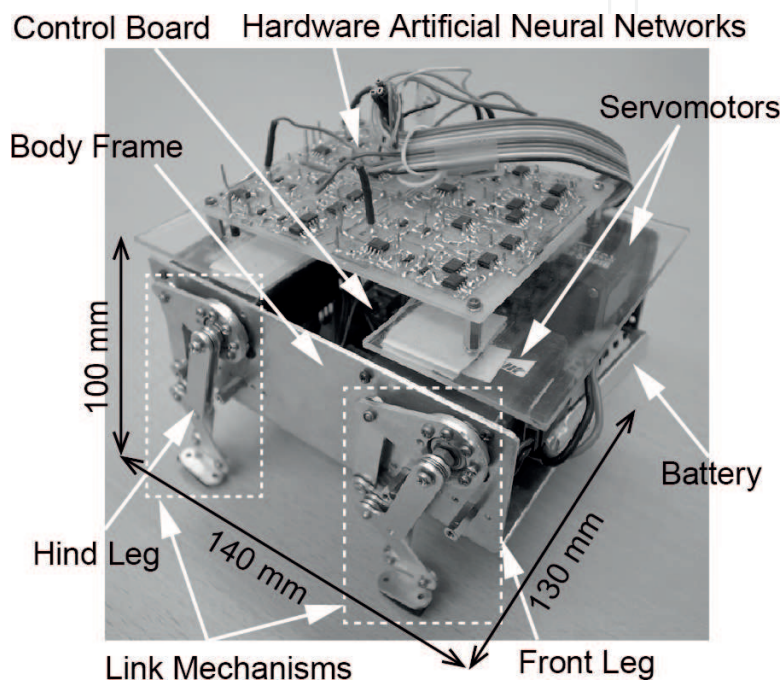
Figure 15. Quadruped robot system mounted with the hardware ANNs as shown in **Figure 14**.
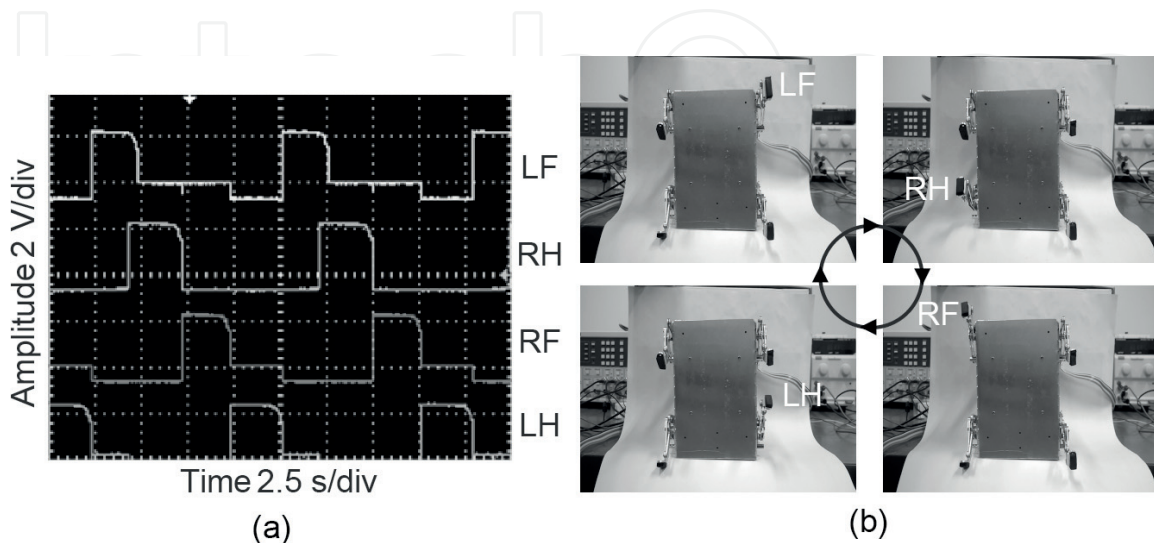
Figure 16. Generated gait pattern and leg motion of a quadruped robot (walk sequence). (a) Waveform and (b) leg motion.

waveform shown in **Figure 16a**, the legs move as shown in **Figure 16b**. In other words, the generated driving rhythm is a four-phase alternating oscillation with the sequence left foreleg (LF), right hindleg (RH), right foreleg (RF), and left hindleg (LH).

The locomotion of a walking quadruped robot driven by the hardware ANNs is captured in **Figure 17**. The motion patterns resemble those of a quadruped animal, thus confirming that the driving rhythms generated by the hardware ANNs can realize proper walking behavior. Moreover, the hardware ANNs can generate various oscillatory patterns without requiring computer programs.

Under an external trigger pulse, the constructed hardware ANNs can change the gait pattern of the quadruped robot. A walk-to-trot gait change is illustrated in **Figure 18**. The external trigger pulse is generated by a waveform generator applied to the input port (see **Figure 10**). Considering that the hardware ANNs can memorize the applied gait rhythm, the quadruped robot can switch its locomotion pattern by applying an external input to its hardware ANNs.

4.2. Locomotion of the hexapod robot

Figure 19 shows the IC of the hardware ANNs. Panel (a) shows the layout pattern of the bare IC chip of the hardware ANNs. The design rule of the bare IC chip is four-metal two-poly CMOS (0.35 μm). The chip is sized (2.45×2.45) mm^2. The hardware ANNs are connected as
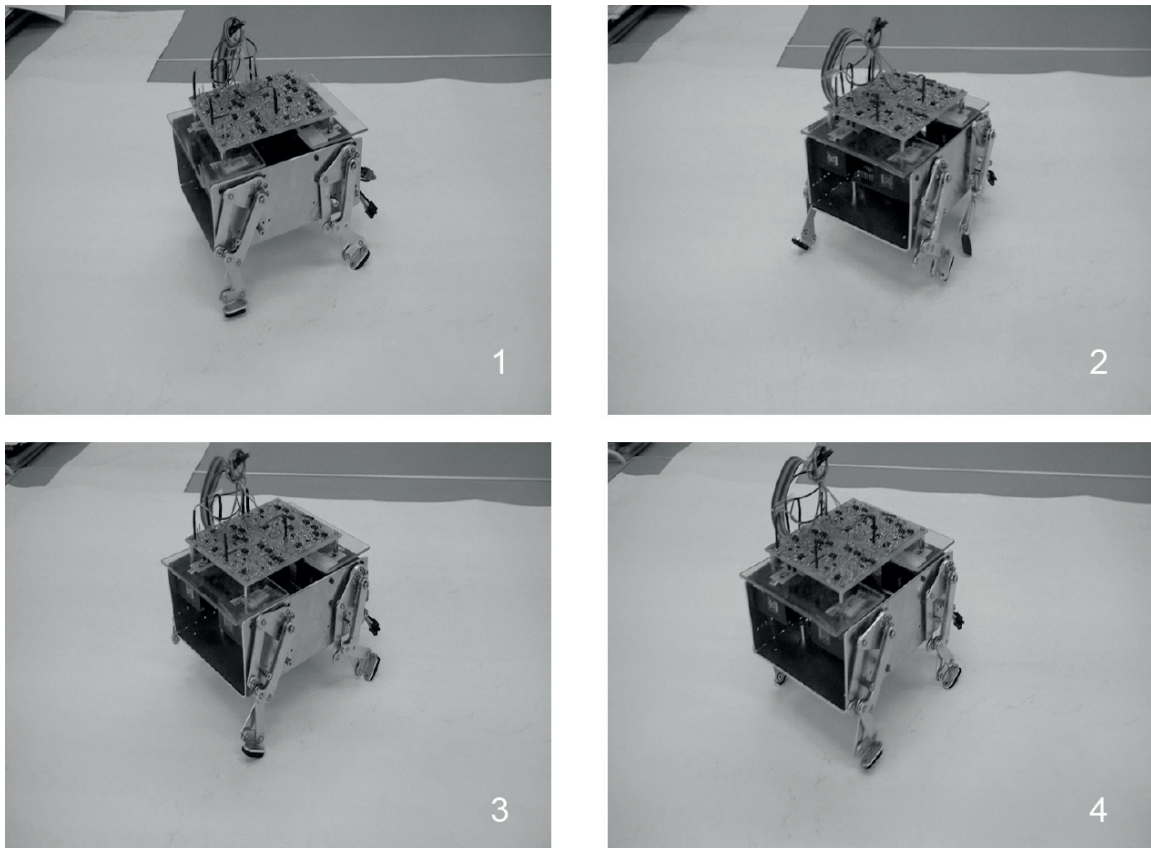

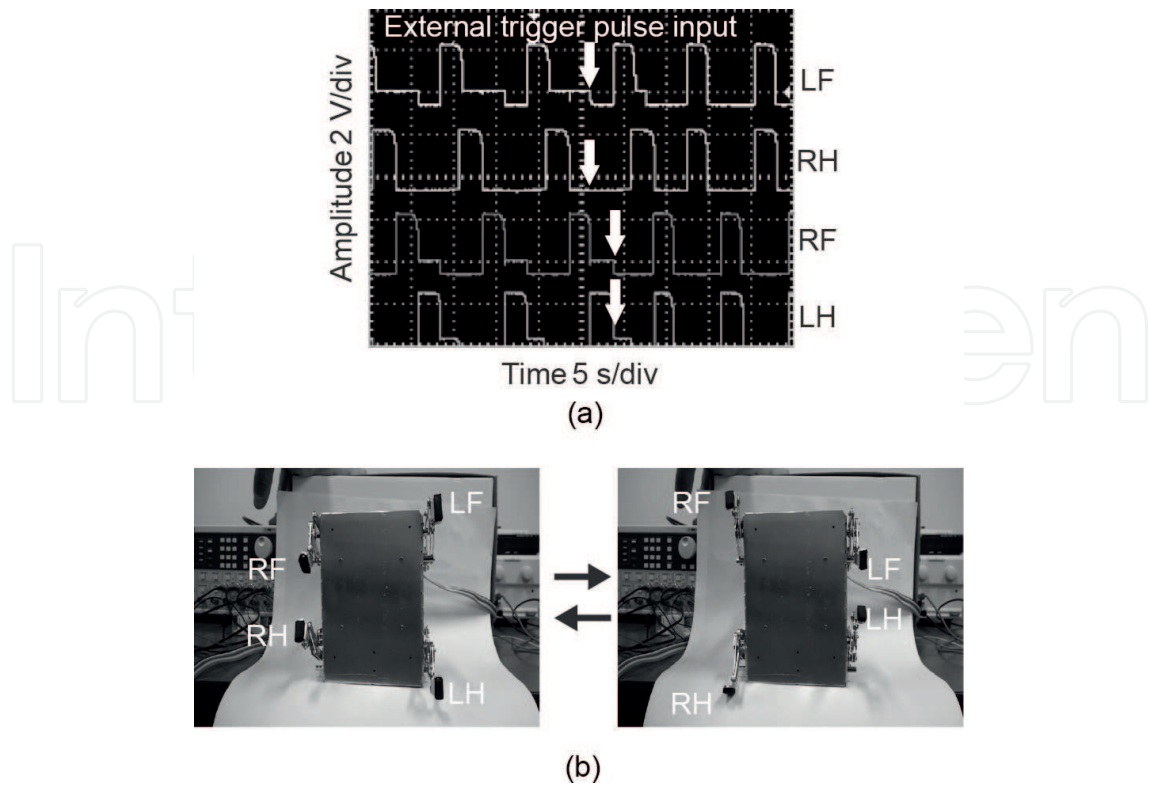**Figure 17.** Locomotion (walk) of the quadruped robot driven by hardware ANNs.

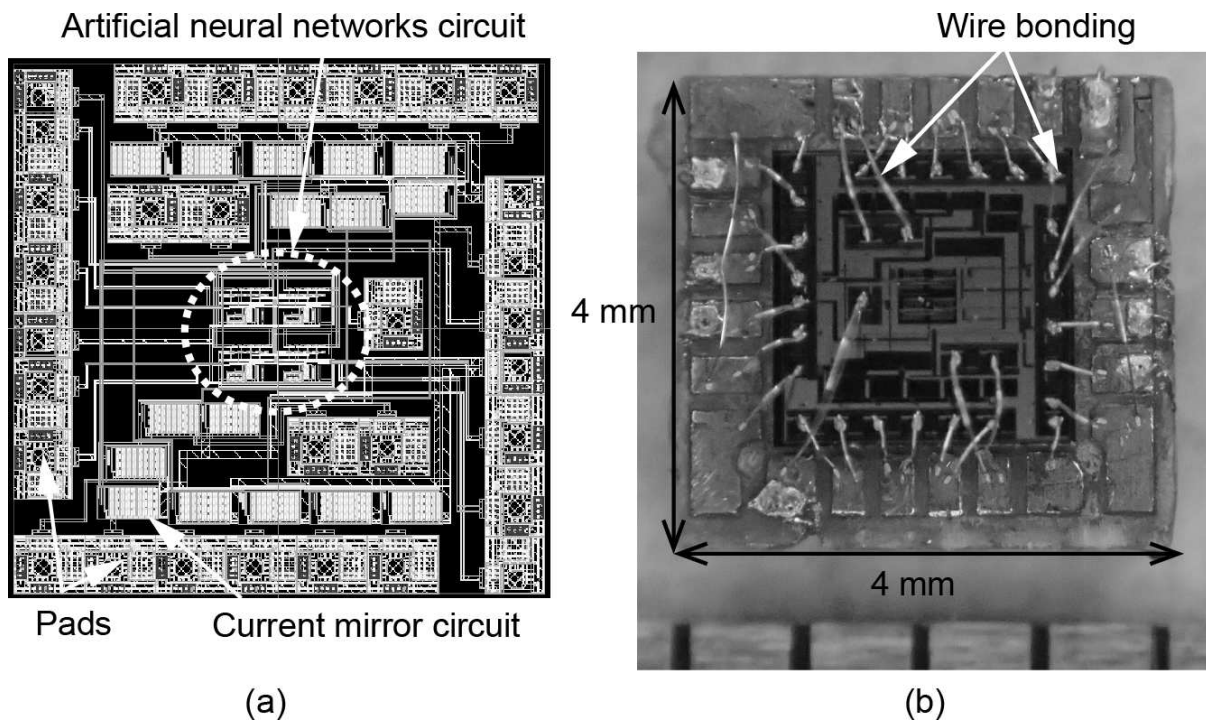**Figure 18.** Example of changing the gait pattern from walk to trot. (a) Waveform and (b) leg motion.

Figure 19. The hardware ANNs are constructed as IC. (a) Layout design and (b) bare IC chip with FR4 circuit board.

shown in **Figure 13**. Four cell body models are mutually coupled by 12 inhibitory synaptic models. The driving waveform of the hexapod robot is generated by the outputs extracted from the hardware ANNs and the current mirror circuit. Four trigger pulse input ports are also extracted from the hardware ANNs. The sequence of the locomotion rhythm depends on the
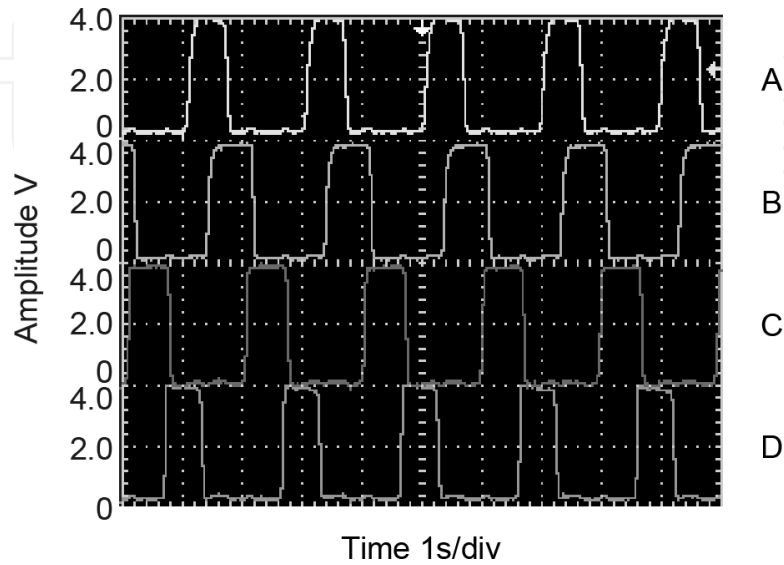

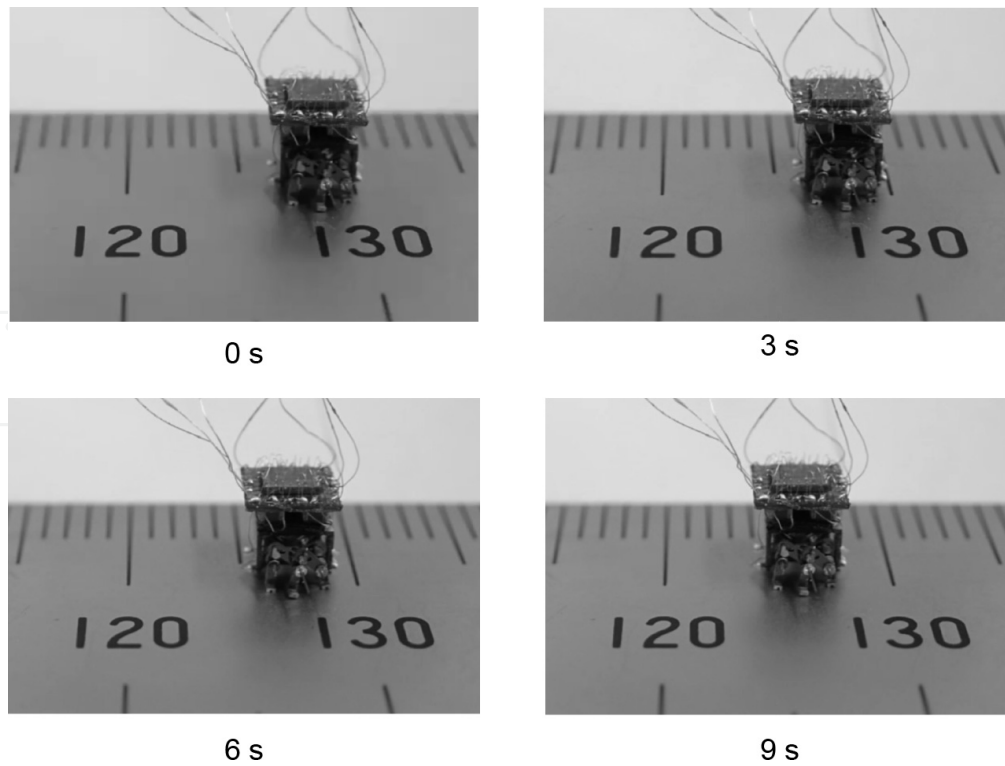**Figure 20.** Measured output waveforms of the designed IC.

Figure 21. Locomotion (walking) of the hexapod robot mounted with the hardware ANNs.

timing of the single external trigger pulse. **Figure 19b** shows the constructed bare IC chip, which is fixed to the cavity of an FR4 circuit board by wire bonding.

Figure 20 shows the measured output waveform of the designed IC. The hardware ANNs can generate the locomotion rhythms observed in living organisms. To sufficiently heat and cool the artificial muscle wires, the pulse width, period, and amplitude were set to 0.5 s, 2 s, and 75 mA, respectively. The connected helical artificial muscle wires are approximately 50 Ω. As shown in **Figure 20**, the output waveform effectively actuates the actuator of the hexapod robot. The approximate power consumptions of the hardware ANNs and the current mirror circuit were 0.708 and 488 mWh, respectively. The former almost matches the power consumption of biological neural networks, but the power consumption of the artificial muscle wire was excessive.

The circuit in **Figure 19b** was mounted on the hexapod robot. **Figure 21** shows snapshots of the walking hexapod robot system. The driving waveforms generated by the hardware ANNs actuate the hexapod robot, thus enabling successful locomotion.

5. Conclusions

This chapter describes the basic characteristics of the hardware ANNs as gait generators of multilegged robots.

The main findings are summarized below.

1. The basic component of the hardware ANN (namely, the cell body model) has the basic features of a class II neuron model.

2. Gait generation by the hardware ANNs uses synchronization phenomena, as observed in biological neural networks.

3. The hardware ANNs successfully guided the locomotion of two types of multilegged robots without requiring software programs or analog digital converters.

Currently, the authors consider replacing the artificial muscle wire by an electrostatic actuator to reduce the actuating power. The electrostatic actuator will be powered by high-voltage silicon photovoltaic cells installed in the microrobot system. In future works, the ANNs, actuator, power source system, and sensory system will be directly integrated into the silicon frame parts of the microrobot.

Author details

Ken Saito[1,2]*, Masaya Ohara[1], Mizuki Abe[3], Minami Kaneko[1] and Fumio Uchikoba[1]

*Address all correspondence to: kensaito@eme.cst.nihon-u.ac.jp

1 Department of Precision Machinery Engineering, College of Science and Technology, Nihon University, Chiba, Japan

2 Department of Mechanical Engineering, University of California, Berkeley, USA

3 Precision Machinery Engineering, Graduate School of Science and Technology, Nihon University, Tokyo, Japan

References

[1] Fujita M, Kitano H. Development of an autonomous quadruped robot for robot entertainment. Autonomous Robots. 1998;**5**:7-18. DOI: 10.1007/978-1-4615-5735-7

[2] Mcghh RB, Iswandhi GI. Adaptive locomotion of a multilegged robot over rough terrain. IEEE Transactions on Systems, Man, and Cybernetics. 1979;**9**(4):176-182. DOI: 10.1109/TSMC.1979.4310180

[3] Raibert M, Blankespoor K, Nelson G, Playter R, The BigDog Team. BigDog, the Rough-Terrain Quadruped Robot. In: Proceedings of the 17th World Congress The International Federation of Automatic Control; July 6–11. Seoul, Korea: Elsevier Ltd; 2008. p. 10822-10825. DOI: 10.3182/20080706–5-KR-1001.01833

[4] Habib MK, Watanabe K, Izumi K. Biomimetics robots: From bio-inspiration to implementation. In: Proceedings of the 33rd Annual Conference of the IEEE Industrial Electronics Society, Nov. 5–8. Taipei, Taiwan: IEEE; 2007. p. 143-148. DOI: 10.1109/IECON.2007.4460382

[5] Habib MK. Biomimetcs: Innovations and Robotics. International Journal of Mechatronics and Manufacturing Systems. 2011;**4**(2):113-134. DOI: 10.1504/IJMMS.2011.039263

[6] Kimura H, Fukuoka Y, Konaga K. Adaptive dynamic walking of a quadruped robot using a neural system model. Advanced Robotics. 2001;**15**(8):859-878. DOI: 10.1163/156855301317198179

[7] Fukuoka Y, Kimura H, Cohen AH. Adaptive dynamic walking of a quadruped robot on irregular terrain based on biological concepts. The International Journal of Robotics Research. 2003;**22**(3–4):187-202. DOI: 10.1177/0278364903022003004

[8] Ijspeert AJ. Central pattern generators for locomotion control in animals and robots: A review. Neural Networks. 2008;**21**(4):642-653. DOI: 10.1016/j.neunet.1 March 2008.4

[9] Schilling M, Hoinville T, Schmitz J, Cruse H. Walknet, a bio-inspired controller for hexapod walking. Biological Cybernetics. 2013;**107**(4):397-419. DOI: 10.1007/s00422-013-0563-5

[10] Schilling M, Paskarbeit J, Huffmeier A, Schneider A, Schmitz J, Cruse H. A hexapod walker using a heterarchical architecture for action selection. Frontiers in Computational Neuroscience. 2013;**7**:1-17/126. DOI: 10.3389/fncom.2013.00126

[11] Delcomyn F. Neural basis of rhythmic behavior in animals. Science. 1980;**210**(4469):492-498. DOI: 10.1126/science.7423199

[12] Arbib MA. The Handbook of Brain Theory and Neural Networks. 2nd ed. Cambridge, MA: The MIT Press; 2002 1308 p

[13] Rinzel J, Ermentrout GB. Analysis of neural excitability and oscillations. In: Koch C, Segev I, editors. Methods in Neuronal Modeling. 2nd ed. Cambridge, MA, The MIT Press; 1998. p. 135-169

[14] Hodgkin AL, Huxley AF. A quantitative description of membrane current and its application to conduction and excitation in nerve. The Journal of Physiology. 1952;**117**(4):500-544

[15] van der Pol B. On "relaxation-oscillations". The London, Edinburgh, and Dublin Philosophical Magazine and Journal of Science. 1926;**2**(11):978–992. DOI: 10.1080/14786442 608564127

[16] Tsumoto K, Yoshinaga T, Aihara K, Kawakami H. Bifurcations in synaptically coupled Hodgkin-Huxley neurons with a periodic input. International Journal of Bifurcation and Chaos. 2003;**13**(3):653-666. DOI: 10.1142/S0218127403006832

[17] Tsumoto K, Yoshinaga T, Iida H, Kawakami H, Aihara K. Bifurcations in a mathematical model for circadian oscillations of clock genes. Journal of Theoretical Biology. 2006;**239**(1): 101-122. DOI: 10.1016/j.jtbi.2005.07.017

[18] Tsuji S, Ueta T, Kawakami H, Aihara K. Bifurcation analysis of current coupled BVP oscillators. International Journal of Bifurcation and Chaos. 2007;**17**(3):837-850. DOI: 10.1142/S0218127407017586

[19] Endo T, Mori S. Mode analysis of a ring of a large number of mutually coupled van der Pol oscillators. IEEE Transactions on Circuits and Systems. 1978;**25**(1):7-18. DOI: 10.1109/TCS.1978.1084380

[20] Kitajima H, Yoshinaga T, Aihara K, Kawakami H. Chaotic bursts and bifurcation in chaotic neural networks with ring structure. International Journal of Bifurcation and Chaos. 2001;**11**(6):1631-1643. DOI: 10.1142/S0218127401002894

[21] Yamauchi M, Wada M, Nishino Y, Ushida A. Wave propagation phenomena of phase states in oscillators coupled by inductors as a ladder. IEICE Transactions on Fundamentals of Electronics, Communications and Computer Sciences. 1999;**E82-A**(11):2592-2598

[22] Yamauchi M, Okuda M, Nishino Y, Ushida A. Analysis of phase-inversion waves in coupled oscillators synchronizing at in-and-anti-phase. IEICE Transactions on Fundamentals of Electronics, Communications and Computer Sciences. 2003;**86-A**(7):1799-1806

[23] Merolla PA, Arthur JV, Alvarez-Icaza R, Cassidy AS, Sawada J, Akopyan F, et al. A million spiking-neuron integrated circuit with a scalable communication network and interface. Science. 2014;**345**(6197):668-673. DOI: 10.1126/science.1254642

[24] Matsuoka J, Sekine Y, Saeki K, Aihara K. Analog hardware implementation of a mathematical model of an asynchronous chaotic neuron. IEICE Transactions on Fundamentals of Electronics, Communications and Computer Sciences. 2002;**E85-A**(2):389-394

[25] Nakabora Y, Saeki K, Sekine Y. Synchronization of coupled oscillators using pulse-type hardware neuron models with mutual coupling. In: Proceedings of the 2004 International Technical Conference on Circuits/Systems; July 6–8. Miyagi, Japan: Computers and Communications; 2004. p. 8D2L-3-1-8D2L-3-4

[26] Saito K, Ikeda Y, Takato M, Uchikoba F. Locomotion rhythm generation using pulse-type hardware neural networks for quadruped robot. In: Ngo TD, editor. Biomimetic Technologies Principles and Applications. 1st ed. Sawston, Cambridge, UK: Woodhead Publishing; 2015. p. 321-334

[27] Saito K, Takato M, Sekine Y, Uchikoba F. MEMS microrobot with pulse-type hardware neural networks integrated circuit. In: Habib MK, editor. Handbook of Research on Advancements in Robotics and Mechatronics. Hershey, PA, USA: IGI Global; 2014. p. 18-35. DOI: 10.4018/978-1-4666-7387-8.ch002

[28] Saito K, Matsuda A, Saeki K, Uchikoba F, Sekine Y. Synchronization of coupled pulse-type hardware neuron models for CPG model. In: Rao AR, Cecchi GA, editors. The Relevance of the Time Domain to Neural Network Models. Boston, MA: Springer; 2012. p. 117-133. DOI: 10.1007/978-1-4614-0724-9_7

[29] Saito K, Takato M, Sekine Y, Uchikoba F. Biomimetics micro robot with active hardware neural networks locomotion control and insect-like switching behaviour. International Journal of Advanced Robotic Systems. 2012;**9**(226):1-6. DOI: 10.5772/54129

[30] Bhardwaj JK, Ashraf H. Advanced silicon etching using high-density plasmas. In: Proceedings SPIE 2639, Micromachining and Microfabrication Process Technology September 19. Austin, TX, USA: SPIE Press; 1995. p. 224-233. DOI: 10.1117/12.221279

[31] Homma D. Metal artificial muscle "BioMetal Fiber". Journal of the Robotics Society of Japan. 2003;**21**(1):22-24. DOI: 10.7210/jrsj.21.22

[32] Toki Corporation. Welcome to Toki Corporation [Internet]. Available from: http://www.toki.co.jp/. [Accessed: July 27, 2017]